MATERIALS SCIENCE

Active nematic emulsions

Pau Guillamat,[1,2] Žiga Kos,[3] Jérôme Hardoüin,[1,2] Jordi Ignés-Mullol,[1,2]* Miha Ravnik,[3,4] Francesc Sagués[1,2]

Copyright © 2018 The Authors, some rights reserved; exclusive licensee American Association for the Advancement of Science. No claim to original U.S. Government Works. Distributed under a Creative Commons Attribution NonCommercial License 4.0 (CC BY-NC).

The formation of emulsions from multiple immiscible fluids is governed by classical concepts such as surface tension, differential chemical affinity and viscosity, and the action of surface-active agents. Much less is known about emulsification when one of the components is active and thus inherently not constrained by the laws of thermodynamic equilibrium. We demonstrate one such realization consisting in the encapsulation of an active liquid crystal (LC)–like gel, based on microtubules and kinesin molecular motors, into a thermotropic LC. These active nematic emulsions exhibit a variety of dynamic behaviors that arise from the cross-talk between topological defects separately residing in the active and passive components. Using numerical simulations, we show a feedback mechanism by which active flows continuously drive the passive defects that, in response, resolve the otherwise degenerated trajectories of the active defects. Our experiments show that the choice of surfactant, which stabilizes the active/passive interface, allows tuning the regularity of the self-sustained dynamic events. The hybrid active-passive system demonstrated here provides new perspectives for dynamic self-assembly driven by an active material but regulated by the equilibrium properties of the passive component.

INTRODUCTION

Emulsions are mixtures of two or more immiscible liquids whose properties are distinctly determined by the interplay between different components across the interface (*1*–*3*). Simple realizations consist in dispersions of aqueous and oily components, with typical examples ranging from food and cosmetic products to drugs and physiological fluids. Emulsion research is nowadays driven by multiple scientific and technological motivations, such as their use as photonic materials (*4*) or as handles for the control of molecular transport (*5*), emulsion stabilization with nanoparticles (*6*), self-assembly of microcapsules (*7*), and reconfigurability via interfacial tunability (*8*). Twenty years ago, a celebrated milestone was reached when a nematic liquid crystal (LC) was used as the dispersing phase (*9*–*11*). From a fundamental point of view, the novelty in these nematic emulsions in relation to traditional preparations comes from the fact that, beyond electric and van der Waals forces, new interactions, originating in the orientational elasticity of the host matrix, come to play a decisive role (*9*, *12*). This development, and the parallel realization involving dispersed solid colloids, has enabled new self-assembling strategies while envisaging the design of composite materials with pre-engineered capacities, such as topologically protected states, fractality, and strong field tunability (*13*–*19*). However, up to now, this approach is purely based on principles of static (equilibrium) self-assembly (*20*). Here, the far-reach idea that we introduce is to change this perspective by demonstrating the realization of active nematic (AN) emulsions whose behavior is not restricted by the laws of equilibrium thermodynamics.

Active systems (*21*, *22*) have been investigated profusely during the past decade, singularly in relation to biologically inspired in vitro realizations (*23*–*25*). A remarkable group of such materials are active gels (*26*, *27*), assembled from bundled microtubules (MTs) cross-linked by kinesin (*23*), that use motor units to transform chemical adenosine 5′-triphosphate (ATP)–based energy into directed flow and microactivity. When condensed at fluid interfaces, this activity organizes spontaneous nematic orientational order of the gel, whose dynamics is characterized by the proliferation of self-propelling defects. Recent studies with planar interfaces reveal that, despite the robustness of these configurations, the dynamics of such AN can be influenced by the rheology of the contacting fluid, and its flow patterns can be conditioned in the presence of anisotropic interfacial stresses (*28*, *29*). When constrained to the surface of a sphere, the tubulin/kinesin AN (*30*) forms a shell whose topology, according to the Gauss-Bonnet theorem, demands the existence of a combined defect charge +2 (*31*, *32*). For small enough droplets, this requirement is met with four +1/2 active defects moving in the cortical shell and displaying, for moderate activities, a periodic dynamic that connects tetrahedral with more energetic coplanar spatial defect arrangements (*30*, *33*).

Here, we report the preparation of AN emulsions, where an aqueous active gel is dispersed into a continuous nematic thermotropic LC. We show that a distinctive feature is the cross-talk between the topological defects of the active and passive components. Using a combination of experiments and numerical simulations, the AN-driven dynamics reveals the emergence of regular and irregular regimes characterized by single, multiple, or broad-spectrum frequencies. The cortical flows triggered by active defects are prolonged into the host matrix, where they distort the passive defect structures. In turn, the latter unevenly distribute viscous stresses on the droplet surface and, in this way, organize the active defect trajectories. Apart from its fundamental interest, the presented scenario points toward the exploration of new modes of dynamic self-assembly, envisaging the realization of functional colloidal soft matter, inherently capable of featuring micromotility, locomotion, and activity.

RESULTS AND DISCUSSION

In our experiments, we emulsify an aqueous kinesin/tubulin active gel within the hydrophobic thermotropic LC 4-pentyl-4-cyanobiphenyl (5CB) (see Fig. 1 and Materials and Methods). Inside the microdroplets, depletion forces push the fluorescently labeled MTs toward the water/5CB interface, leading to the formation of an AN shell onto the inner surface of the droplets (Fig. 2, A to C). Within a few minutes, all the MTs have migrated to the interface, whereas the bulk contains a diluted active

[1]Department of Materials Science and Physical Chemistry, University of Barcelona, Martí i Franquès 1, 08028 Barcelona, Catalonia. [2]Institute of Nanoscience and Nanotechnology, IN2UB, University de Barcelona, Barcelona, Catalonia. [3]Faculty of Mathematics and Physics, University of Ljubljana, Jadranska 19, 1000 Ljubljana, Slovenia. [4]Jozef Stefan Institute, Jamova 39, 1000 Ljubljana, Slovenia.
*Corresponding author. Email: jignes@ub.edu

Downloaded from http://advances.sciencemag.org/ on April 7, 2018

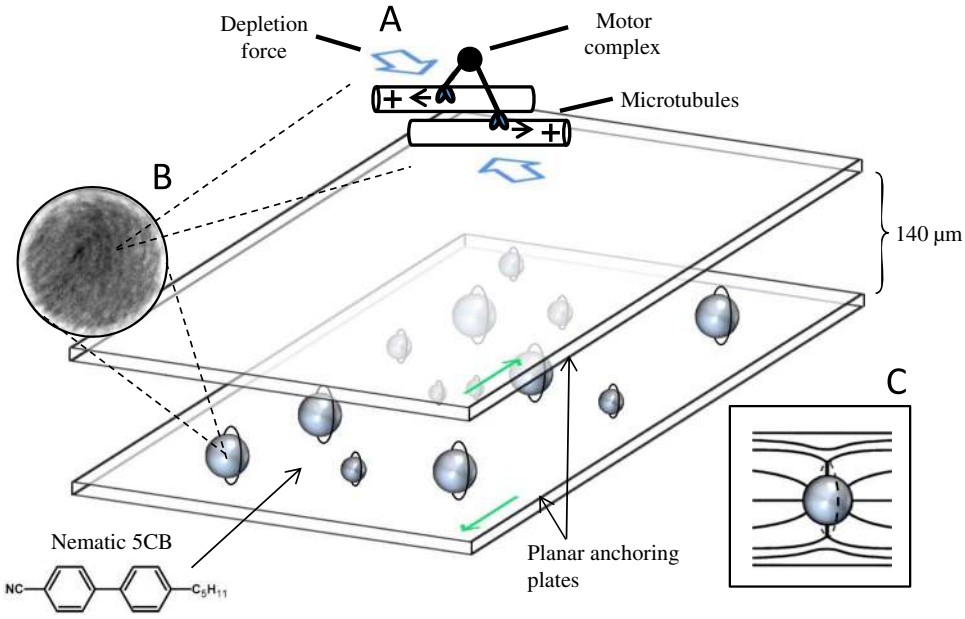

Fig. 1. Scheme of the experimental setup. Flow cells composed of unidirectionally rubbed (green arrows) polyvinyl alcohol (PVA)–coated glass plates confine the emulsions, where the LC 5CB disperses droplets of a tubulin/kinesin-based active gel (**A**). The latter condenses at the water/LC interface in the form of an AN shell (fluorescence micrograph) (**B**). The LC anchoring conditions on the spherical droplets lead to the formation of Saturn ring (SR) defects (**C**).

gel that provides with a reservoir of ATP, enzymes, and motors required for the self-sustained motion of the AN shell. Fluorescence microscopy is used to visualize the structure of the active phase, whereas polarizing and bright-field microscopies are used to observe the passive mesogen (see Materials and Methods). Fluorescence confocal microscopy reveals that the shell is a few micrometers thick (fig. S1). Although recent experiments have revealed that, under confinement, the bulk active gel can develop self-sustained ordered flows (*34*), the fact that, here, most of the filaments concentrate at the water/oil interface allows assuming that residual bulk active flows will be irrelevant compared with flows generated by the active shell.

Net topological charge of defects in a thin nematic shell is +2, which is, because of energetics of the nematic, typically realized by four +1/2 defects; however, AN shells may, in principle, feature more than four topological defects. As a matter of fact, the steady-state defect spacing in an AN layer is only related to an activity-dependent length scale (*29*, *35*). Therefore, ANs confined to large droplets are unstable to the bending instability of active filaments, and pairs of positive and negative defects can spontaneously form and proliferate as observed at planar interfaces (*29*, *35*–*38*). On the other hand, droplets that are too small cannot accommodate the four +1/2 demanded by topology, thus preventing the formation of the stable shell. Here, we study droplets 60 to 120 μm in diameter where the AN shell features four +1/2 defects.

We placed the active emulsions in the 140-μm gap between two parallel glass plates treated to impose a homogeneous in-plane alignment of the passive 5CB nematic phase (see Materials and Methods). At the outer droplet surface, the otherwise uniform 5CB matrix develops topological defects due to the spherical inclusion (*39*). When the droplets are stabilized with a PEGylated phospholipid (see Materials and Methods), 5CB molecules organize perpendicularly to the droplet surface (homeotropic anchoring). This results in the formation of a localized ring disclination of quadrupolar character (*40*–*42*), known as Saturn ring (SR). The SR is in a plane perpendicular to the far-field alignment direction of 5CB and wraps the droplet (Figs. 1 and 2A). Bright-field and fluorescence imaging (Fig. 2, D and E, respectively) permit to track at any time the behavior of the SR disclination and to monitor the dynamics of defects in the active nematic (AN) shell, although only two of the four +1/2 active defects can, at most, be observed simultaneously.

While continuously dragged by the inner cortical flows, SRs exhibit a remarkable integrity as they develop deformation modes that are steadily driven by the dynamics of the active defects. In Fig. 2G (see also movies S1 and S2), we show a sequence of snapshots of an SR with a deformation mode that features two maxima and two minima in the transversal distortion. These oscillations can be very stable and regular, spanning dozens of cycles, only limited by the available chemical fuel encapsulated within the aqueous droplet (Fig. 3, A to D). The structure of the deformation modes may be characterized either by a single mode (Figs. 2G and 3A) or by a superposition of a main mode and its harmonics (Fig. 3, E and F, and movie S3). As we discuss below, the type of dynamic behavior is determined by the strength of the coupling between the active and the passive phases and by the geometrical arrangements of the active defects with respect to the outer ring disclination.

For the studied size range, about 10% of the droplets feature oscillating SRs when sample monitoring begins, which typically corresponds to an elapsed time of about 10 min since emulsion preparation. The rest of the droplets exhibit a dipolar arrangement as a result of the collapse of the SR into a bulk point defect (hedgehog) (*43*), a configuration that is also compatible with the homeotropic anchoring of the passive nematic. The SR is not stable in the presence of active flow and is susceptible to degenerate into this dipolar configuration. Although such folding can occur spontaneously in the presence of nonactive inclusions (*41*), we find that the lifetime of the oscillating SR decreases markedly with the activity of the AN shell. This lifetime is just a few minutes for high activity but more than 1 hour for low-activity regimes (fig. S2). In the latter case,

Downloaded from http://advances.sciencemag.org/ on April 7, 2018

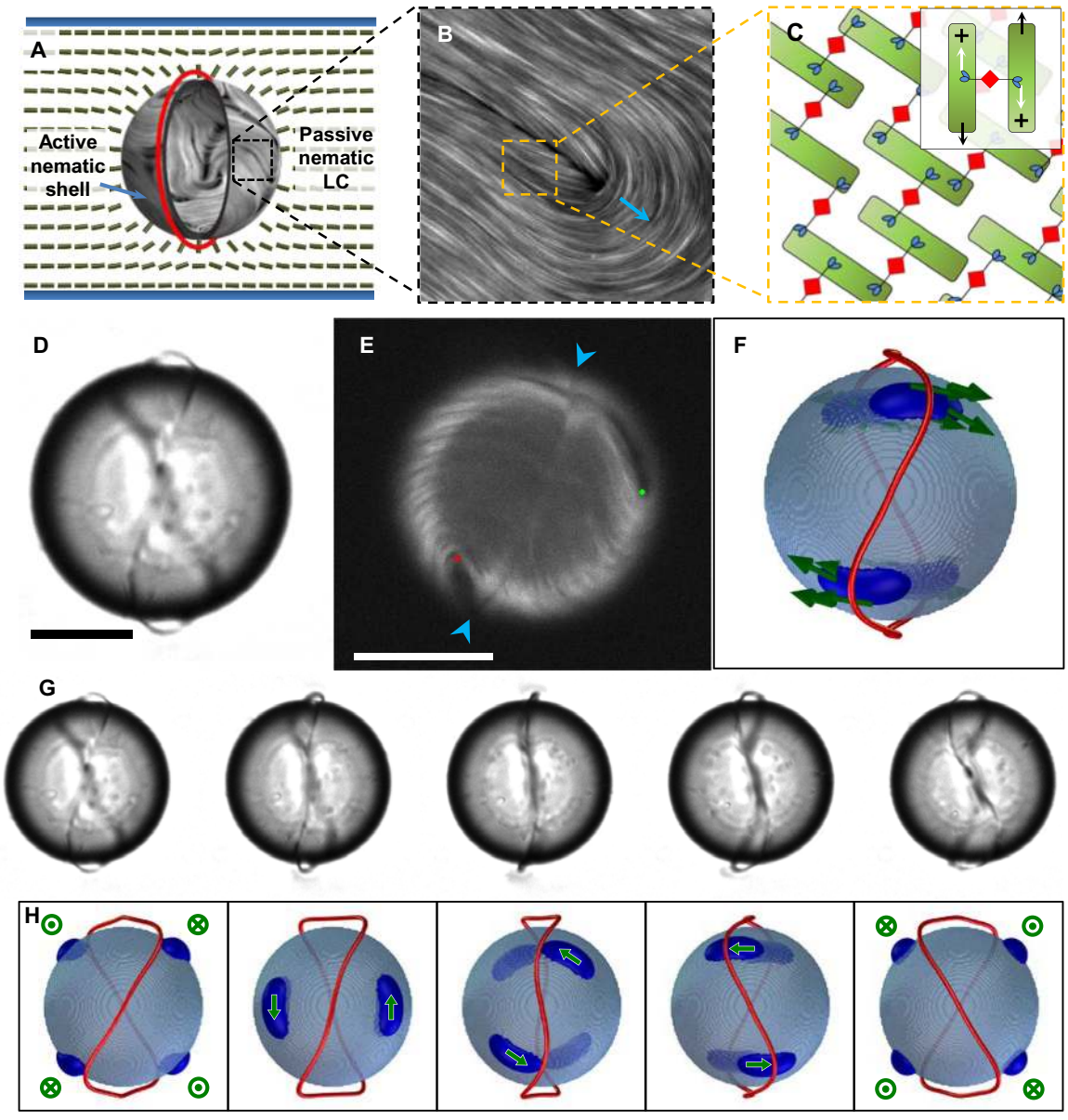

Fig. 2. Periodically oscillating SR. (**A**) Scheme of an AN shell (fluorescence micrograph) in a passive nematic LC. The spherical inclusion deforms the director field (green rods) triggering the generation of an SR disclination (red ring). (**B**) High magnification of a +1/2 defect in the AN. Field of view is 20 μm wide. For extensile systems, these defects self-propel in the tail-to-head direction (blue arrow). (**C**) Schematic of the active material. Bundles of MTs (green rods) are internally cross-linked by molecular motor clusters, based on two kinesin proteins linked by a streptavidin molecule (in red). When bound to MTs of opposite polarities, molecular motor clusters exert shear forces within the bundles (inset). White arrows indicate the direction of motion of the molecular motors along the filaments, whereas black arrows show the sense of motion of the filaments. (**D**) Bright-field micrograph of an oscillating SR at the maximum amplitude of the oscillations. (**E**) Fluorescence micrographs allow simultaneous visualization of both the active shell and the SR surrounding it. The SR is subtended between the two blue arrowheads, and it is dragged by two active defects, whose tips are marked by a dot. (**F**) Snapshot of a simulated SR in the oscillating state (scalar order parameter drawn at $S = 0.4$). Velocity field (green arrows) in the passive nematic and isosurface of its magnitude ($v = 310\ \xi_N/t_0$ in blue; see also Materials and Methods), indicating the position of the active defects. An image sequence showing a half-period of the oscillation of an SR is shown for experiments (**G**) and for simulations (**H**). Scale bars, 50 μm. See movies S1 and S2.

the SR may never collapse simply because activity ends before this event occurs, because of ATP exhaustion.

To better understand the coupling between the active and the passive defect motion, we performed numerical simulations, which we found to consistently reproduce the observed single-mode SR oscillations (Fig. 2, F and H, and movie S1). The central assumption of the model is that the back coupling of the passive dispersing material in response to the motion of active defects is weak enough not to cause major deformations of the active trajectories. This assumption allows us to consider trajectories in our case similar to those described by Zhang *et al.* (*33*) for free active droplets (fig. S3). The motion of the defects in the active shell is characterized by the transition between a slightly distorted tetrahedral configuration and a higher-energy planar arrangement, with a periodic evolution between the two. Simulations

Downloaded from http://advances.sciencemag.org/ on April 7, 2018

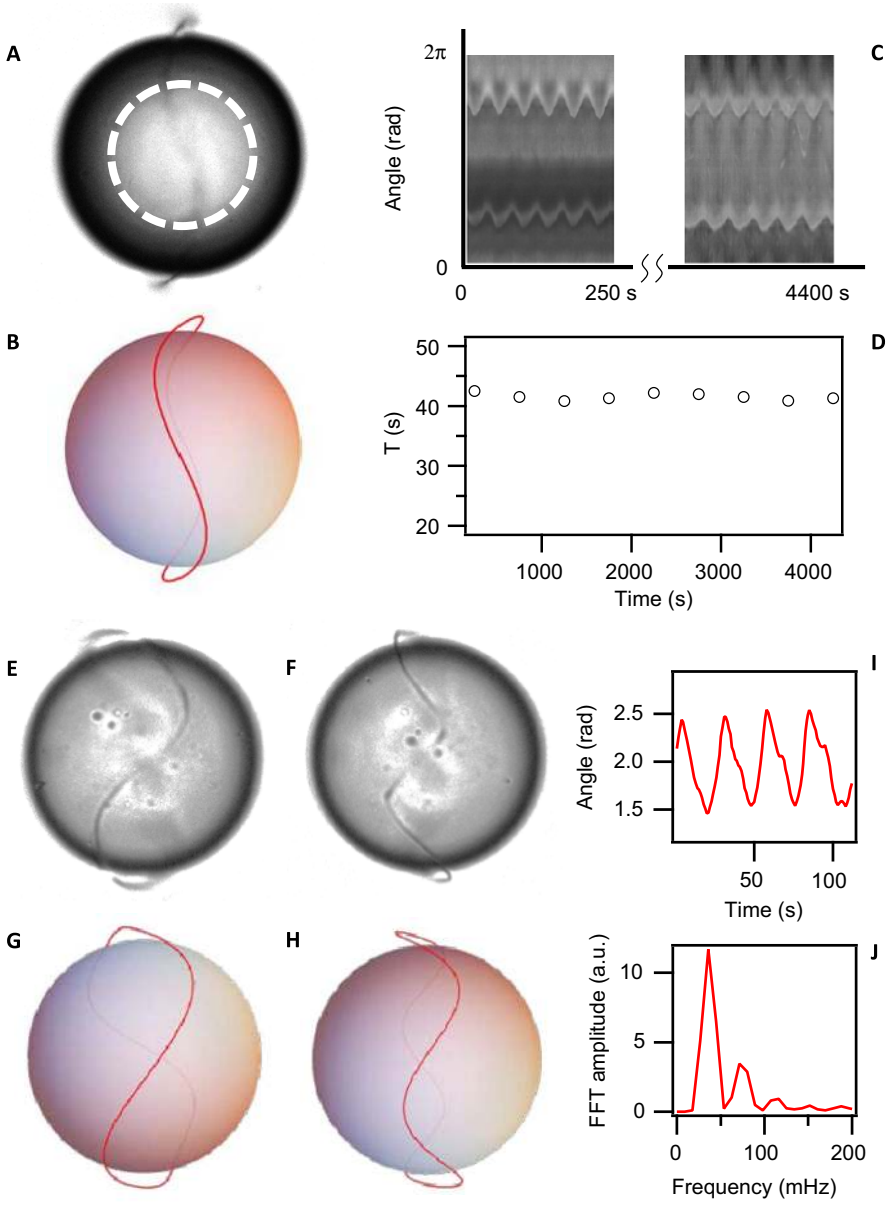

Fig. 3. Persistence of the oscillating SRs. (**A**) Bright-field image of a single-mode oscillating SR around a droplet with a diameter of 83 μm. (**B**) Sketch showing an SR with an $n = 3$ deformation mode. (**C**) Space-time plot along the dashed circumference in (A). (**D**) Average period of the oscillations over a 250-s interval at different times. (**E** and **F**) Bright-field image of a multimode oscillating SR with a diameter of 127 μm (see movie S3). The elapsed time between the two snapshots is 9 s. (**G** and **H**) Sketch showing SR with a combination of $n = 2$ and $n = 4$ deformation modes, corresponding to the phase of the SRs in (E) and (F), respectively. (**I**) Tracking of the angular position of the SR along an $r = 40$ μm circumference. (**J**) Fast Fourier transform (FFT) power spectrum of the trace in (I). a.u., arbitrary units.

reveal that one period of the SR oscillations corresponds to multiple transitions between the two active defect configurations (fig. S4).

The high symmetry of the sphere and the corresponding freedom in inscribing the embedded cube anticipate a high degeneracy of the realized trajectories. Simulations show that a key variable to explain the dynamical regime is the orientation of the active defect trajectories with respect to the equilibrium plane, perpendicular to the passive nematic far field (Fig. 4, A and B). Figure 4A shows an aligned situation, where active defects rotate in pairs around the x, y, and z axis, oscillating between a coplanar and a tetrahedron-like configuration. Notice that, in this aligned configuration, the active defects lie on the plane of the SR in one of the coplanar configurations. We have probed the response of the passive nematic to the alignment of active trajectories by rotating the latter around the z axis so that that coplanar configuration now forms an angle β with respect to the plane of the SR (Fig. 4B). For consistency, we have also run numerical simulations for active trajectories being rotated around the x or y axis, obtaining similar conclusions as with rotations around the z axis. Whereas the plane of the SR is set by the strong boundary conditions imposed by the cell walls on the passive LC, the orientation of the four active defects is, in principle, degenerate. Our simulations show that the single-mode oscillations of the SR observed in the experiments are reproduced only for β close to zero (Fig. 4, E and F),

Downloaded from http://advances.sciencemag.org/ on April 7, 2018

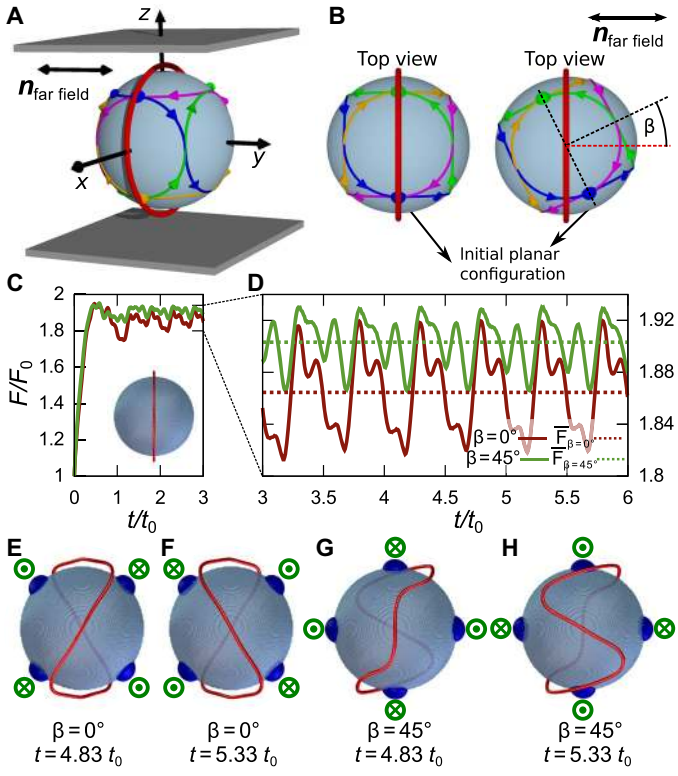

Fig. 4. Coupling of the active defect trajectories to the passive nematic. (**A**) Arrows indicate the periodic active defect trajectories prescribed in the simulations and their orientation with respect to the passive nematic far field in a system confined between two planes that are perpendicular to the *z* axis. (**B**) Schematics of the defect trajectories projected on the *xy* plane. Defects are depicted in the coplanar configuration, which defines the angle β, relative to the SR. (**C** and **D**) Simulations allow computing the passive nematic elastic energy as a function of time (in units of active defect oscillation period, t_0) for β = 0° and β = 45°, starting from the undistorted SR configuration [inset in (C)]. (**E** to **H**) Numerical investigation of the influence of β on the dynamics of the SR. Snapshots of the defect structure for β = 0° (E and F) and β = 45° (G and H). Snapshots (E to H) reveal that single-mode oscillations of the SR as observed in Fig. 2 can be only reproduced for β = 0° (see movie S4).

whereas for nonzero values of β, the SR displays high-mode or multimode oscillations (Fig. 4, G and H, and movie S4). As a consequence, a situation where the orientation of the oscillating active defects were truly degenerate should result in a negligible fraction of droplets with β ≃ 0. The fact that our experiments revealed the existence of droplets with SRs featuring simple deformation modes (on average, a little less than half of the dozens of tested droplets exhibiting stable SRs) indicates that there is a feedback between the passive LC and the AN shell that leads to the orientation of the active defects toward the β ≃ 0 configuration. We propose that hydrodynamic coupling can mediate in this cross-talk between active and passive LCs, because one can expect that the drag forces and corresponding viscous stresses felt by the active shell will be different in droplet regions near the ring disclination. Our simulations also demonstrate that a configuration with β ≃ 0 is energetically favorable for the oscillating SR. Figure 4 (C and D) depicts the oscillating trend of the elastic energy of the passive LC, showing that β = 0 indeed corresponds to an elastic nematic free-energy landscape with deeper minima.

Droplets where the SR is less than 1 μm from the active shell were marginally stable with respect to the collapse into the dipolar configuration (fig. S2). Monitoring these droplets allowed observing the transition between the different dynamic regimes of the oscillating SR (Fig. 5 and movie S5). The single-mode oscillating SR (Fig. 5A) could evolve, sometimes reversibly, into multimode oscillating regimes (Fig. 5B). The dominant modes of the sustained oscillations are highlighted by the Fourier analysis of the average transmitted intensity in polarized microscopy images (Fig. 5, F and G). Our simulations (fig. S3 and movie S6) revealed that these multimode oscillations could be obtained with active defects that broke, even if only once, the regularity of the orbits to follow a new set of trajectories, when moving between two coplanar positions. After such event, defects still moved along the same lines but with reverse directions with respect to the original orbits. This is further shown in fig. S3.

Eventually, the SR became highly distorted and practically dismantled (Fig. 5C). During the sequence of transitions, the signature of periodic oscillations faded away (Fig. 5, E to G), converting the original spectrum with a single frequency peak into a multiple peak and, finally, a noisy spectrum. This is an indication that emulsions of active and passive components can sustain mutually coupled randomly evolving regimes that are characterized by a broad frequency distribution of dynamic behavior. Eventually, this highly convoluted dynamic phase led irreversibly to the final, lower-energy dipolar configuration (Fig. 5D).

In the reported experiments, the amplitude and the dominant deformation mode in SRs increased with the activity of the AN and with the strength of the coupling between the AN and the passive phase. Activity can be modified via ATP concentration, but we did not use this as a control parameter after observing that active flows were more vigorous in some droplets of analogous size, presumably because of a heterogeneous partition of the aqueous active phase during the droplet-forming process. On the other hand, coupling strength will be higher when the disclination is closer to the droplet surface, taking into account the flow pattern in the passive phase unveiled by our simulations (fig. S5). The distance from the SR to the surface typically scales with the droplet radius (*40*), although it depends on the strength of the surface anchoring given by the surfactant (*44*). In our experiments, we observed a significant variability in the equilibrium SR position for droplets of similar size, which may again point to a heterogeneous partition of the water-dispersed surfactant during the emulsification process, leading to a dispersion in the anchoring strength.

By changing the type of surfactant stabilizing the active emulsion, one can easily tune the anchoring conditions of the passive LC at the surface of the droplets, thus imposing different topological constraints on the motion of active defects. In particular, interesting effects may arise from the coupling of active flows with less labile passive defect configurations, such as the recently reported hexadecapolar structure (*45*), composed of a simultaneous pair of point-like surface point defects (boojums) and an SR disclination that is obtained for conical anchoring at the droplet surface. Here, we induce this configuration around the active shells by using the surfactant Tween 80 (see Materials and Methods). As a result, we obtain highly regular oscillatory regimes that are remarkably stable over time (Fig. 6 and movie S7). This could be interpreted as arising from a higher constrainment on the SR disclination due to the presence of the pair of quasi-immobile boojums.

CONCLUSION

In summary, we have reported from experiments and numerical simulations a scenario of cross-talk between active and passive defects when

Downloaded from http://advances.sciencemag.org/ on April 7, 2018

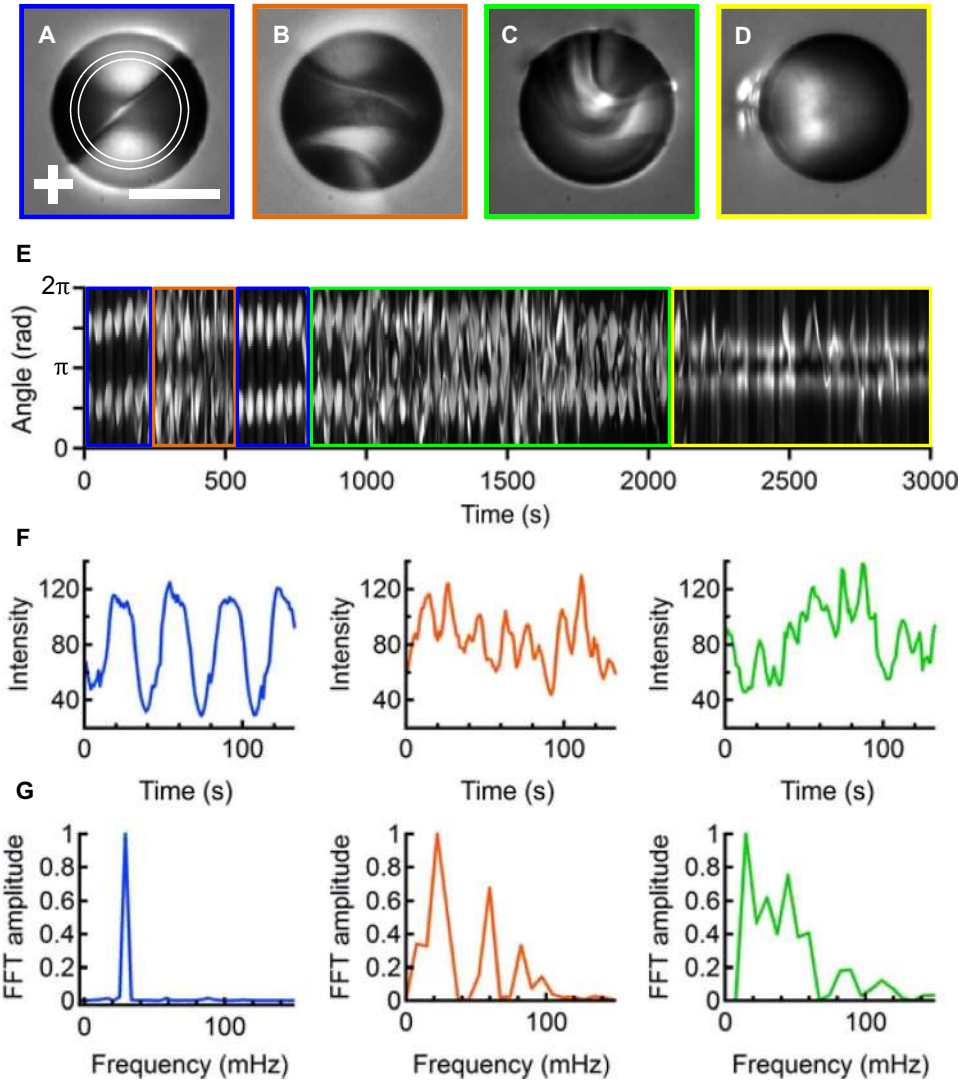

Fig. 5. Dynamic regimes of the AN emulsion. Polarization micrographs for single-mode oscillating (**A**), multimode oscillating (**B**), highly distorted or chaotic (**C**), and collapsed, effectively dipolar (**D**) SR configurations of the same droplet (see movie S5). The orientation of the polarizers is represented by the white cross. Scale bar, 50 μm. (**E**) Space-time plot corresponding to the region within the ring depicted in (A) for an image sequence showing the SR evolution over time. Frame colors relate with the corresponding SR configurations shown in (A) to (D). (**F**) Plot profiles of the average grayscale intensity inside the ring-shaped region over time. Crossed-polarized observation allows highlighting the dynamical features of the SR. Trace colors correspond to the different SR dynamic regimes in (E). (**G**) FFT amplitude of the oscillations in (F).

droplets containing active shells are dispersed in a passive LC. This supposes an unprecedented realization in the hierarchy of emulsion-based soft matter systems that combines active lyotropic and passive thermotropic LCs. By tracking the behavior of SR-localized disclinations in the host matrix, we identify a wealth of dynamical regimes induced by the sustained cortical flows. Strikingly enough, when the periodically visited trajectories of active defects are compatible with the SR structure, the paths of the active defects appear locked while inducing periodic oscillations of the SR. This situation is, however, prone to destabilization, giving rise to chaotic regimes, or even to the change of the passive defect structure. The dynamic regime depends on the coupling between the active and passive phases, in particular, on the nature and concentration of the surfactant that determines the boundary conditions of the passive mesogen. A tight control of the system, especially if one aims at the realization of a homogeneous active emulsion, will require the implementation of microfluidic techniques that allow surpassing the heterogeneous partition of the active aqueous preparation observed in the reported experiments.

From a fundamental point of view, our study is an alternative to and complements recent experiments on bacteria dispersed in lyotropic LCs (*46*–*48*) and should foster the incipient research on active droplets (*49*–*53*). In a broader perspective, our research can be related to the propulsion of emulsified droplets embedded in either isotropic (*54*) or anisotropic environments (*55*) that, so far, have not involved an inherently active component.

Beyond its fundamental interest, the research reported here opens new perspectives by extending from isolated to ensembles of active droplets. Designing strategies of dynamic self-assembly based on these active units may provide with new tools to engineer materials powered by biological energy.

Downloaded from http://advances.sciencemag.org/ on April 7, 2018

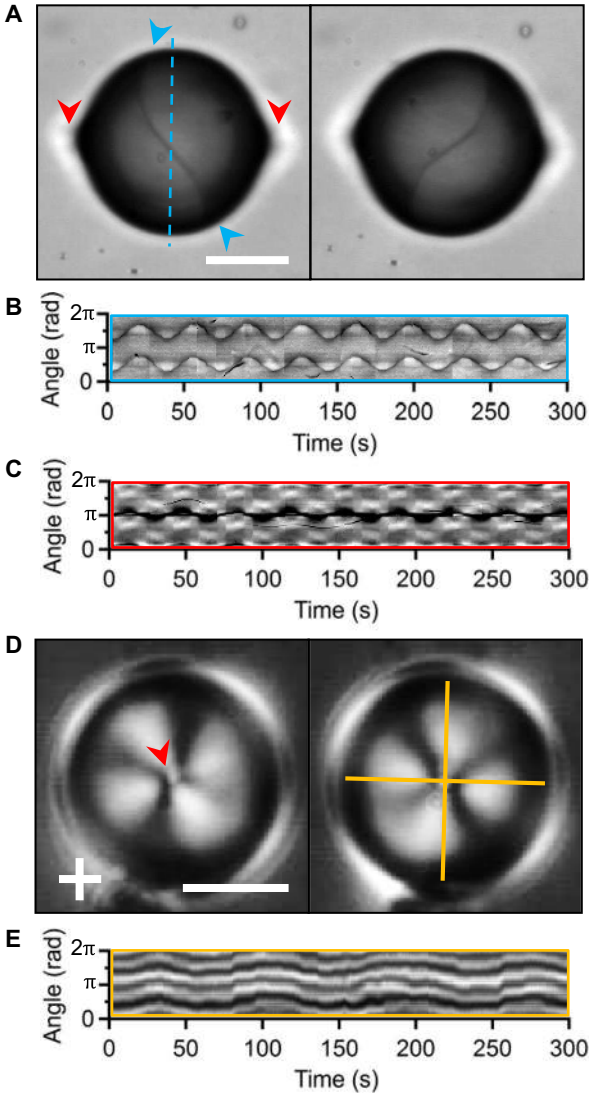

Fig. 6. Oscillation in hexadecapolar configurations of the passive nematic. (**A**) Bright-field micrographs show the evolution of an activated hexadecapolar passive nematic configuration, formed by an SR and two surface point defects (boojum). Blue arrowheads indicate the position of the SR, which oscillates far from the equilibrium position (blue dashed line). Although boojums remain pinned at their location (red arrows), they also exhibit oscillations. (**B** and **C**) Space-time plots show the regular oscillating behavior of all defects. (**D**) Using homeotropic anchoring of the LC at the bounding plates, the plane of the SR is parallel to the plane of the sample. In the polarizing micrographs, the red arrowhead indicates the position of the boojum defect closest to the top plate. The orange cross indicates the equilibrium position for the four oscillating black brushes (**E**). The white cross indicates the orientation of the polarizers. Scale bars, 50 μm (see movie S7).

MATERIALS AND METHODS

Materials

Purification of tubulin

Heterodimeric (α,β)-tubulin (obtained from the Brandeis University Biological Materials Facility) was purified from bovine brain tissue through two cycles of polymerization/depolymerization in high-molarity Pipes buffer (*56*).

Polymerization of MTs

Tubulin was incubated at 37°C for 30 min in an M2B buffer (80 mM Pipes, 1 mM EGTA, and 2 mM $MgCl_2$) (P1851, E3889, and M4880, respectively; Sigma) supplemented with the reducing agent dithiothreitol (DTT) (0.4 mM; 43815, Sigma) and with guanosine-5-[(α, β)-methyleno] triphosphate (GMPCPP) (0.6 mM; NU-405, Jena Biosciences), a non-hydrolyzable analog of the nucleotide guanosine 5′-triphosphate. By controlling the concentration of GMPCPP, we were able to prepare high-density suspensions of short MTs (1 to 2 μm). For the characterization with fluorescence microscopy, part of the initial tubulin (3%) was fluorescently labeled with Alexa Fluor 647 (A20006, Thermo Fisher Scientific), which is attached by a succinimidyl ester linker to a primary amine on the tubulin surface. After incubation, MT suspensions were allowed to sit at room temperature for 5 hours. Subsequently, they were aliquoted in small volumes, snap-frozen in liquid nitrogen, and kept at −80°C.

Kinesin expression

Drosophila melanogaster heavy-chain kinesin-1 (K401-BCCP-6His) has been expressed in *Escherichia coli* by using the plasmid WC2 from The Gelles Laboratory (Brandeis University, MA, USA) and purified with a nickel column (*57*). In brief, a single *E. coli* colony was grown in LB broth. Subsequently, expression was induced by adding isopropyl-β-D-thiogalactopyranoside in the culture, which was kept shaking at 22°C overnight. After pelleting cells by centrifugation, the pellet was resuspended in a lysis buffer and sonicated. Subsequent ultracentrifugation allowed getting the expressed protein in the low-speed supernatant, which was loaded into a nickel column for purification. After dialysis against 500 mM imidazole, a desalting column was used to exchange the buffer to 50 mM Hepes buffer solution. The protein was concentrated with a molecular exclusion column, and its concentration was estimated by means of absorption spectroscopy. Finally, kinesin was stored at a specific concentration in a 40% (w/v) sucrose solution at −80°C.

Preparation of kinesin clusters

Biotinylated kinesin motor proteins and tetrameric streptavidin (43-4301, Invitrogen), supplemented with the reducing agent DTT (0.1 mM), were incubated on ice for 30 min at a stoichiometric ratio of 2:1 to obtain kinesin-streptavidin motor clusters.

Active gel assembly

MTs were mixed with the molecular motor clusters that act as active cross-linkers and with ATP (A2383, Sigma) that drives the activity of the gel. The aqueous dispersion contains a nonadsorbing polymer [polyethylene glycol (PEG), 20 kDa; 95172, Sigma] that promotes the formation of filament bundles via depletion interaction. To maintain a constant concentration of ATP during the experiments, we added an enzymatic ATP-regenerator system based on phosphoenolpyruvate (P7127, Sigma) and pyruvate kinase (434301, Invitrogen), which converted adenosine 5′-diphosphate back into ATP. Several antioxidant components were also included in the solution to prevent protein residues from forming disulfide bonds and to minimize fluorophore damage by oxygen species. The antioxidants were as follows: Trolox (238813, Sigma), DTT (43815, Sigma), and an oxygen-scavenging enzymatic mixture that includes glucose (G8270, Sigma), glucose oxidase (G2133, Sigma), and catalase (C1345, Sigma).

Surfactants

A PEGylated surfactant must be added in the active mixture to procure biocompatible water/oil interfaces in subsequent steps. For these experiments, which involve water/LC interfaces, the choice of surfactant also determines the disposition of the LC molecules at the interface with the active aqueous suspension. For planar anchoring, Pluronic F-127 [1 to 3% (w/v); P2443, Sigma] was used, and for conic anchoring,

Downloaded from http://advances.sciencemag.org/ on April 7, 2018

Tween 80 [5 to 10% (w/v); P4780, Sigma] was used. For homeotropic anchoring of the mesogen molecules, we used three types of modified phospholipids with a 2000-Da PEG moiety in the polar head, namely, 1,2-distearoyl-*sn*-glycero-3-phosphoethanolamine-*N*-[methoxy(polyethylene glycol)-2000] ammonium salt (DSPE-PEG1; 880120, Avanti Polar Lipids), 1,2 distearoyl-*sn*-glycero-phosphoethanolamine-*N*-[amino(polyethylene glycol)-2000] ammonium salt (DSPE-PEG2; 880128, Avanti Polar Lipids), and 1,2-distearoyl-*sn*-glycero-3-phosphoethanolamine-*N*-[dibenzocyclooctyl(polyethylene glycol)-2000] ammonium salt (DSPE-PEG3; 880229, Avanti Polar Lipids). Every surfactant was first dissolved in chloroform/methanol (2:1 v/v) with a final concentration of 25 mg/ml. The lipid solution was then dried for 20 min under a gentle N_2 stream, followed by 1 hour under vacuum. The dry lipid cake was then hydrated for 1 hour to a final concentration of 12.5 mg/ml in a phosphate buffer [20 mM K_2PO_4 + 100 mM KCl (pH 7.4)]. Vesicles spontaneously form after a few cycles of sonication and mixing, giving the solution a milky aspect. The suspensions were stored below room temperature and sonicated for a few seconds before their use. Lipid vesicles were dispersed in the aqueous active solution to achieve a final lipid concentration of 0.2% (w/v).

Active LC-based emulsions

Mechanical mixing of the active suspension (supplemented with a surfactant) in the thermotropic LC oil 5CB (ST00683, Synthon Chemicals) in a volumetric ratio of 1:30 led to the formation of active water-in-LC emulsions. To enhance the homeotropic anchoring around the active gel aqueous droplets, we doped 5CB with 15 mM stearic acid (S4751, Sigma). The latter was first dissolved in chloroform at 42.5 mg/ml. This solution was mixed with 5CB in a volumetric ratio of 1:10. The chloroform was removed by heating the mix at 60°C under vacuum overnight and cooled under a gentle N_2 stream for 30 min.

LC cells

Active emulsions were confined between parallel plates that set equal anchoring conditions to the molecules of the continuous mesophase, either planar or homeotropic. Rubbed PVA (146 to 186 kDa; 363103, Sigma) spin-coated glass plates were used to induce unidirectional planar anchoring. Conversely, glass substrates functionalized with a fluoroalkyl silane (Aquapel, PPG Industries) imposed perpendicular anchoring of the LCs. Two sheets of double-sided tape, used as spacers between the plates, ensured a separation of 140 μm. After being filled by capillarity, the cell was sealed using ultraviolet-curable epoxy glue (NOA81, Norland Optical).

Sample characterization

Polarization, bright-field, and fluorescence microscopies have been used to characterize the active emulsions. Polarized light- and bright-field microscopies were performed with a Nikon Eclipse 50iPol upright microscope. Images were acquired with an AVT Marlin 131B complementary metal-oxide semiconductor digital video camera. Observation of active samples based on fluorescently labeled MTs was carried out with the same microscope, which is also equipped with a white light-emitting diode light source epiilluminator (MWWHLP1, Thorlabs) and a Cy5 fluorescence filter set (Edmund Optics). Image acquisition was performed with an Andor iXon 877 cooled electron multiplying charge-coupled device and Andor Zyla 4.2 Plus cameras, both operated with ImageJ Micro-Manager open-source software.

Analysis of the defect dynamics

Image analysis of the passive LC dynamics was performed with custom-written ImageJ plugins, which extract space-time plots from a ring-shaped selection. FFTs were calculated from the oscillations of the average grayscale intensity.

Numerical simulations

We performed numerical simulations of a passive nematic driven by the dynamics of an AN shell. The process of a simulation could be roughly divided into three steps: First, position and orientation of active defects in time were chosen to correspond to the trajectories published in the previous investigations of AN shells. Second, a velocity profile on an active shell was calculated from the position and orientation of active defects. Third, a velocity profile on an active shell was used as a boundary condition for a full simulation of a passive nematic dynamics.

AN defect trajectories

First experimental realization of AN shells have revealed a complex dynamics of four + 1/2 nematic defects, based on their oscillation between coplanar and tetrahedral configurations (*30*). Numerical simulations (*33*) capture coplanar-tetrahedral oscillations, in which active defects are not bounded in pairs. We approximated the numerical results by constructing active defect orbits from a set of circular arches, which lie on an intersection between a sphere and a cube (fig. S3A). The defects were propagated along the trajectories with a constant velocity and oscillated between coplanar and tetrahedron-like configurations (fig. S3B). Furthermore, such approximation allows capturing the irregular behavior (fig. S3C) observed in numerical simulations of active shells at higher activity (*33*).

Velocity profile on active shells

An AN profile of a + 1/2 defect on a plane generates a force field (*58*)

$$\mathbf{f} = \frac{\alpha}{2r}\hat{\mathbf{x}} \tag{1}$$

where α is the activity, r is the distance from the defect, and $\hat{x}$ is the orientation of the defect. We used stereographic projection to map a force distribution due to active defects on a shell and calculated the velocity profile on a spherical shell using a lattice Boltzmann method with isotropic viscosity. The obtained results show the velocity profile with clear peaks at the positions of active defects (fig. S6) and well-formed flow structures, such as vortices (fig. S6A) and stagnation points (fig. S6B).

Passive nematic dynamics

Our numerical simulations are based on the Beris-Edwards approach to nematodynamics (*59*), where the evolution of the system density ρ, velocity **v**, and full nematic tensor order parameter **Q** are described by the continuity, Navier-Stokes, and nematic tensor nematodynamic equations

$$\partial_t \rho + \nabla \cdot (\rho \mathbf{v}) = 0 \tag{2a}$$

$$\rho(\partial_t + \mathbf{v} \cdot \nabla)\mathbf{v} = \nabla \cdot \boldsymbol{\sigma} \tag{2b}$$

$$(\partial_t + \mathbf{v} \cdot \nabla)\mathbf{Q} - \mathbf{S} = \Gamma \mathbf{H} \tag{2c}$$

where **H** is the molecular field tensor

$$\mathbf{H} = -\frac{\delta \mathcal{F}_{\mathrm{LdG}}}{\delta \mathbf{Q}} + \frac{1}{3}\mathrm{Tr}\left(\frac{\delta \mathcal{F}_{\mathrm{LdG}}}{\delta \mathbf{Q}}\right)\mathbf{I} \tag{3}$$

Downloaded from http://advances.sciencemag.org/ on April 7, 2018

with

$$\mathcal{F}_{\mathrm{LdG}} = \int \mathrm{d}V \left[\frac{A}{2}\mathrm{Tr}\,\mathbf{Q}^2 + \frac{B}{3}\mathrm{Tr}\,\mathbf{Q}^3 + \frac{C}{4}(\mathrm{Tr}\,\mathbf{Q}^2)^2\right] + \frac{L}{2}\int \mathrm{d}V\,|\nabla\mathbf{Q}|^2 + \frac{W}{2}\int \mathrm{d}A\,\mathrm{Tr}(\mathbf{Q}-\mathbf{Q}_0)^2 \quad (4)$$

the Landau-de Gennes free energy expanded by the surface anchoring energy with preferred tensor order parameter $\mathbf{Q}_0$. A, B, and C are material parameters determining the nematic degree of order, L is the elastic constant, and W is the anchoring strength. The generalized advection term $\mathbf{S}$ couples the nematic orientation to the flow

$$\mathbf{S} = (\xi\mathbf{u}-\boldsymbol{\omega})\cdot\left(\mathbf{Q}+\frac{1}{3}\mathbf{I}\right) + \left(\mathbf{Q}+\frac{1}{3}\mathbf{I}\right)\cdot(\xi\mathbf{u}+\boldsymbol{\omega}) - 2\xi\left(\mathbf{Q}+\frac{1}{3}\mathbf{I}\right)\mathrm{Tr}(\mathbf{Q}\cdot\nabla\mathbf{v}) \quad (5)$$

where $u_{ij} = (\partial_i v_j + \partial_j v_i)/2$ and $\omega_{ij} = (\partial_i v_j - \partial_j v_i)/2$ are the strain rate and vorticity tensor, respectively, and ξ is the alignment parameter. The stress tensor $\boldsymbol{\sigma}$ is given by

$$\boldsymbol{\sigma} = -\left(P_0 - \frac{L}{2}|\nabla\mathbf{Q}|^2\right)I + 2\eta\mathbf{u} - \xi\mathbf{H}\cdot\left(\mathbf{Q}+\frac{1}{3}\mathbf{I}\right) - \xi\left(\mathbf{Q}+\frac{1}{3}\mathbf{I}\right)\cdot\mathbf{H} + 2\xi\left(\mathbf{Q}+\frac{1}{3}\mathbf{I}\right)\mathrm{Tr}(\mathbf{Q}\cdot\mathbf{H}) + \mathbf{Q}\cdot\mathbf{H} - \mathbf{H}\cdot\mathbf{Q} + \boldsymbol{\sigma}^{\mathrm{E}} \quad (6)$$

where $\sigma^{\mathrm{E}}_{ij} = -\partial_j Q_{kl}\frac{\delta\mathcal{F}_{\mathrm{LdG}}}{\delta\partial_j Q_{kl}}$. For all practical purposes, pressure contribution P_0 can be assumed constant throughout the sample. The values for the parameters used in the simulations are given in the units of elastic constant L, rotational viscosity parameter Γ, and nematic correlation length $\xi_N = \left[L/\left(A + BS_0 + 9CS_0^2/2\right)\right]^{1/2}$, where $S_0 = 0.533$ is the equilibrium degree of nematic order: $A = -0.189L/\xi_N^2$, $B = -2.33L/\xi_N^2$, $C = 1.90L/\xi_N^2$, $W = 0.829L/\xi_N$, and $\eta = 1.37/\Gamma$, $\xi = 0.942$. The radius of the active shell equals $75.4\xi_N$, and the period of the active defect oscillation is $t_0 = 948\xi_N^2/L\Gamma$. The size of the simulation box is $332\xi_N \times 332\xi_N \times 231\xi_N$ with no-slip velocity boundary condition and fixed director field at the sides of the simulation box. Equations 2a to 2c were numerically integrated using a hybrid lattice Boltzmann approach, consisting of a finite difference method for the evolution of the nematic tensor order parameter (Eq. 2c) and a lattice Boltzmann method (*60*, *61*) with a 19-velocity lattice model, Bhatnagar-Gross-Krook collision operator, and a moving boundary at the interface with the active shell for the Navier-Stokes (Eq. 2b) and the continuity (Eq. 2a) equations.

SUPPLEMENTARY MATERIALS

Supplementary material for this article is available at http://advances.sciencemag.org/cgi/content/full/4/4/eaao1470/DC1

fig. S1. Thickness of the AN layer.
fig. S2. Long-term stability of the SRs.
fig. S3. Trajectories of the active defects in a spherical shell used in the numerical simulations.
fig. S4. Connection between active and passive phases.
fig. S5. An example of the velocity field of the passive LC as generated by active defect motion.
fig. S6. Snapshots of a velocity profile in an active shell.
movie S1. Oscillatory dynamics of an SR defect.
movie S2. Active defects drive the SR oscillations.
movie S3. Multimode oscillations of an SR.
movie S4. Defect dynamics at different β angles.
movie S5. Dynamic regimes of the SRs.
movie S6. Simulation of a multimode oscillating regime of the SR.
movie S7. Dynamic hexadecapolar configuration.

REFERENCES AND NOTES

1. T. F. Tadros, *Emulsion Formation, Stability, and Rheology* (Wiley-VCH Verlag GmbH & Co. KGaA, 2013).
2. E. Dickinson, Food emulsions and foams: Stabilization by particles. *Curr. Opin. Colloid Interface Sci.* **15**, 40–49 (2010).
3. G. T. Vladisavljevi, R. A. Nuumani, S. A. Nabavi, Microfluidic production of multiple emulsions. *Micromachines* **8**, 75 (2017).
4. S. Nagelberg, L. D. Zarzar, N. Nicolas, K. Subramanian, J. A. Kalow, V. Sresht, D. Blankschtein, G. Barbastathis, M. Kreysing, T. M. Swager, M. Kolle, Reconfigurable and responsive droplet-based compound micro-lenses. *Nat. Commun.* **8**, 14673 (2017).
5. P. Gruner, B. Riechers, B. Semin, J. Lim, A. Johnston, K. Short, J. C. Baret, Controlling molecular transport in minimal emulsions. *Nat. Commun.* **7**, 10392 (2016).
6. K. Kim, S. Kim, J. Ryu, J. Jeon, S. G. Jang, H. Kim, D.-G. Gweon, W. B. Im, Y. Han, H. Kim, S. Q. Choi, Processable high internal phase Pickering emulsions using depletion attraction. *Nat. Commun.* **8**, 14305 (2017).
7. C. H. J. Evers, J. A. Luiken, P. G. Bolhuis, W. K. Kegel, Self-assembly of microcapsules via colloidal bond hybridization and anisotropy. *Nature* **534**, 364–368 (2016).
8. L. D. Zarzar, V. Sresht, E. M. Sletten, J. A. Kalow, D. Blankschtein, T. M. Swager, Dynamically reconfigurable complex emulsions via tunable interfacial tensions. *Nature* **518**, 520–524 (2015).
9. P. Poulin, H. Stark, T. C. Lubensky, D. A. Weitz, Novel colloidal interactions in anisotropic fluids. *Science* **275**, 1770–1773 (1997).
10. J.-C. Loudet, P. Barois, P. Poulin, Colloidal ordering from phase separation in a liquid-crystalline continuous phase. *Nature* **407**, 611–613 (2000).
11. J. Yamamoto, H. Tanaka, Transparent nematic phase in a liquid-crystal-based microemulsion. *Nature* **409**, 321–325 (2001).
12. T. A. Wood, J. S. Lintuvuori, A. B. Schofield, D. Marenduzzo, W. C. K. Poon, A self-quenched defect glass in a colloid-nematic liquid crystal composite. *Science* **334**, 79–83 (2011).
13. A. Martinez, H. C. Mireles, I. I. Smalyukh, Large-area optoelastic manipulation of colloidal particles in liquid crystals using photoresponsive molecular surface monolayers. *Proc. Natl. Acad. Sci. U.S.A.* **108**, 20891–20896 (2011).
14. R. P. Trivedi, I. I. Klevets, B. Senyuk, T. Lee, I. I. Smalyukh, Reconfigurable interactions and three-dimensional patterning of colloidal particles and defects in lamellar soft media. *Proc. Natl. Acad. Sci. U.S.A.* **109**, 4744–4749 (2012).
15. B. Senyuk, Q. Liu, S. He, R. D. Kamien, R. B. Kusner, T. C. Lubensky, I. I. Smalyukh, Topological colloids. *Nature* **493**, 200–205 (2013).
16. A. Martinez, M. Ravnik, B. Lucero, R. Visvanathan, S. Žumer, I. I. Smalyukh, Mutually tangled colloidal knots and induced defect loops in nematic fields. *Nat. Mater.* **13**, 258–263 (2014).
17. A. Eremin, P. Hirankittiwong, N. Chattham, H. Nádasi, R. Stannarius, J. Limtrakul, O. Haba, K. Yonetake, H. Takezoe, Optically driven translational and rotational motions of microrod particles in a nematic liquid crystal. *Proc. Natl. Acad. Sci. U.S.A.* **112**, 1716–1720 (2015).
18. Q. Liu, P. J. Ackerman, T. C. Lubensky, I. I. Smalyukh, Biaxial ferromagnetic liquid crystal colloids. *Proc. Natl. Acad. Sci. U.S.A.* **113**, 10479–10484 (2016).
19. C. Peng, T. Turiv, Y. Guo, S. V. Shiyanovskii, Q.-H. Wei, O. D. Lavrentovich, Control of colloidal placement by modulated molecular orientation in nematic cells. *Sci. Adv.* **2**, e1600932 (2016).
20. G. M. Whitesides, B. Grzybowski, Self-assembly at all scales. *Science* **295**, 2418–2421 (2002).
21. S. Ramaswamy, The mechanics and statistics of active matter. *Annu. Rev. Condens. Matter Phys.* **1**, 323–345 (2010).
22. M. C. Marchetti, J. F. Joanny, S. Ramaswamy, T. B. Liverpool, J. Prost, M. Rao, R. Aditi Simha, Hydrodynamics of soft active matter. *Rev. Mod. Phys.* **85**, 1143–1189 (2013).
23. T. Sanchez, D. T. N. Chen, S. J. DeCamp, M. Heymann, Z. Dogic, Spontaneous motion in hierarchically assembled active matter. *Nature* **491**, 431–434 (2012).
24. S. Köhler, V. Schaller, A. R. Bausch, Structure formation in active networks. *Nat. Mater.* **10**, 462–468 (2011).
25. Y. Sumino, K. H. Nagai, Y. Shitaka, D. Tanaka, K. Yoshikawa, H. Chaté, K. Oiwa, Large-scale vortex lattice emerging from collectively moving microtubules. *Nature* **483**, 448–452 (2012).
26. F. Julicher, K. Kruse, J. Prost, J. F. Joanny, Active behavior of the cytoskeleton. *Phys. Rep.* **449**, 3–28 (2007).

Downloaded from http://advances.sciencemag.org/ on April 7, 2018

27. J. Prost, F. Jlicher, J. F. Joanny, Active gel physics. *Nat. Phys.* **11**, 111–117 (2015).
28. P. Guillamat, J. Ignés-Mullol, F. Sagués, Control of active liquid crystals with a magnetic field. *Proc. Natl. Acad. Sci. U.S.A.* **113**, 5498–5502 (2016).
29. P. Guillamat, J. Ignés-Mullol, F. Sagués, Taming active turbulence with patterned soft interfaces. *Nat. Commun.* **8**, 564 (2017).
30. F. C. Keber, E. Loiseau, T. Sanchez, S. J. DeCamp, L. Giomi, M. J. Bowick, M. C. Marchetti, Z. Dogic, A. R. Bausch, Topology and dynamics of active nematic vesicles. *Science* **345**, 1135–1139 (2014).
31. T. Lopez-Leon, V. Koning, K. B. S. Devaiah, V. Vitelli, A. Fernandez-Nieves, Frustrated nematic order in spherical geometries. *Nat. Phys.* **7**, 391–394 (2011).
32. H. Shin, M. Bowick, X. Xing, Topological defects in spherical nematics. *Phys. Rev. Lett.* **101** 037802 (2008).
33. R. Zhang, Y. Zhou, M. Rahimi, J. J. de Pablo, Dynamic structure of active nematic shells. *Nat. Commun.* **7**, 13483 (2016).
34. K.-T. Wu, J. B. Hishamunda, D. T. N. Chen, S. J. DeCamp, Y. W. Chang, A. Fernández-Nieves, S. Fraden, Z. Dogic, Transition from turbulent to coherent flows in confined three-dimensional active fluids. *Science* **355**, eaal1979 (2017).
35. L. Giomi, Geometry and topology of turbulence in active nematics. *Phys. Rev. X* **5**, 031003 (2015).
36. S. P. Thampi, R. Golestanian, J. M. Yeomans, Instabilities and topological defects in active nematics. *EPL (Europhys. Lett.)* **105**, 18001 (2014).
37. L. M. Pismen, Dynamics of defects in an active nematic layer. *Phys. Rev. E Stat. Nonlin. Soft Matter Phys.* **88**, 050502 (2013).
38. S. J. DeCamp, G. S. Redner, A. Baskaran, M. F. Hagan, Z. Dogic, Orientational order of motile defects in active nematics. *Nat. Mater.* **14**, 1110–1115 (2015).
39. H. Stark, Physics of colloidal dispersions in nematic liquid crystals. *Phys. Rep.* **351**, 387–474 (2001).
40. O. V. Kuksenok, R. W. Ruhwandl, S. V. Shiyanovskii, E. M. Terentjev, Director structure around a colloid particle suspended in a nematic liquid crystal. *Phys. Rev. E* **54**, 5198–5203 (1996).
41. Y. Gu, N. Abbott, Observation of Saturn-ring defects around solid microspheres in nematic liquid crystals. *Phys. Rev. Lett.* **85**, 4719–4722 (2000).
42. H. Stark, Saturn-ring defects around microspheres suspended in nematic liquid crystals: An analogy between confined geometries and magnetic fields. *Phys. Rev. E* **66**, 032701 (2002).
43. I. Muševic, M. Škarabot, U. Tkalec, M. Ravnik, S. Žumer, Two-dimensional nematic colloidal crystals self-assembled by topological defects. *Science* **313**, 954–958 (2006).
44. P. Oswald, P. Pieranski, *Nematic and Cholesteric Liquid Crystals: Concepts and Physical Properties Illustrated by Experiments* (Liquid Crystals Book Series, Taylor & Francis, 2005).
45. B. Senyuk, O. Puls, O. M. Tovkach, S. B. Chernyshuk, I. I. Smalyukh, Hexadecapolar colloids. *Nat. Commun.* **7**, 10659 (2016).
46. S. Zhou, A. Sokolov, O. D. Lavrentovich, I. S. Aranson, Living liquid crystals. *Proc. Natl. Acad. Sci. U.S.A.* **111**, 1265–1270 (2014).
47. P. C. Mushenheim, R. R. Trivedi, S. S. Roy, M. S. Arnold, D. B. Weibel, N. L. Abbott, Effects of confinement, surface-induced orientations and strain on dynamical behaviors of bacteria in thin liquid crystalline films. *Soft Matter* **11**, 6821–6831 (2015).
48. C. Peng, T. Turiv, Y. Guo, Q.-H. Wei, O. D. Lavrentovich, Command of active matter by topological defects and patterns. *Science* **354**, 882–885 (2016).
49. E. Tjhung, D. Marenduzzo, M. E. Cates, Spontaneous symmetry breaking in active droplets provides a generic route to motility. *Proc. Natl. Acad. Sci. U.S.A.* **109**, 12381–12386 (2012).
50. J.-F. Joanny, S. Ramaswamy, A drop of active matter. *J. Fluid Mech.* **705**, 46–57 (2012).
51. C. A. Whitfield, D. Marenduzzo, R. Voituriez, R. J. Hawkins, Active polar fluid flow in finite droplets. *Eur. Phys. J. E Soft Matter* **37**, 8 (2014).
52. L. Giomi, A. DeSimone, Spontaneous division and motility in active nematic droplets. *Phys. Rev. Lett.* **112**, 147802 (2014).
53. D. Khoromskaia, G. P. Alexander, G. P. Alexander, Motility of active fluid drops on surfaces. *Phys. Rev. E Stat. Nonlin. Soft Matter Phys.* **92**, 062311 (2015).
54. S. Herminghaus, C. C. Maass, C. Krüger, S. Thutupalli, L. Goehring, C. Bahr, Interfacial mechanisms in active emulsions. *Soft Matter* **10**, 7008–7022 (2014).
55. S. Hernández-Navarro, P. Tierno, J. A. Farrera, J. Ignés-Mullol, F. Sagués, Reconfigurable swarms of nematic colloids controlled by photoactivated surface patterns. *Angew. Chem. Int. Ed. Engl.* **53**, 10696–10700 (2014).
56. M. Castoldi, A. V. Popov, Purification of brain tubulin through two cycles of polymerization–depolymerization in a high-molarity buffer. *Protein Expr. Purif.* **32**, 83–88 (2003).
57. R. Subramanian, J. Gelles, Two distinct modes of processive kinesin movement in mixtures of ATP and AMP-PNP. *J. Gen. Physiol.* **130**, 445–455 (2007).
58. L. Giomi, M. J. Bowick, P. Mishra, R. Sknepnek, M. C. Marchetti, Defect dynamics in active nematics. *Philos. Trans. A Math. Phys. Eng. Sci.* **372**, 20130365 (2014).
59. A. N. Beris, B. J. Edwards, *Thermodynamics of Flowing Systems: With Internal Microstructure* (Oxford Engineering Science Series, Oxford Univ. Press, 1994).
60. C. Denniston, E. Orlandini, J. M. Yeomans, Lattice Boltzmann simulations of liquid crystal hydrodynamics. *Phys. Rev. E Stat. Nonlin. Soft Matter Phys.* **63**, 056702 (2001).
61. S. Succi, *The Lattice Boltzmann Equation for Fluid Dynamics and Beyond* (Clarendon Press, 2001).

Acknowledgments: We are indebted to the Brandeis University Materials Research Science and Engineering Centers (MRSEC) Biosynthesis facility for providing the tubulin. We thank M. Pons, A. LeRoux, and G. Iruela (University of Barcelona) for assistance in the expression of motor proteins. **Funding:** Ž.K. and M.R. acknowledge funding from Slovenian Research Agency through grants P1-0099, J1-7300, and L1-8135 and United States Air Force Research Laboratory European Office of Aerospace Research and Development research project Nematic Colloidal Tilings as Tunable Soft Metamaterials (grant no. FA9550-15-1-0418). P.G., J.H., J.I.-M., and F.S. acknowledge funding from Ministerio de Economia, Industria y Competitividad, Spain (project FIS2016-78507-C2-1-P, Agencia Estatal de Investigación/ European Regional Development Fund). P.G. acknowledges funding from Generalitat de Catalunya through a PhD Fellowship. J.H. acknowledges funding from the European Union's Horizon 2020 research and innovation program under grant agreement no. 674979-NANOTRANS. Brandeis University MRSEC Biosynthesis facility is supported by NSF MRSEC DMR-1420382. J.I.-M. and F.S. thank University of Barcelona for contributing to the author production costs of the manuscript. **Author contributions:** P.G., J.I.-M., and F.S. conceived the experiments. P.G. and J.H. performed the experiments and analysis of experimental data. Ž.K. and M.R. conducted the numerical simulations. J.I.-M., M.R., and F.S. wrote the manuscript with contribution from all the authors. **Competing interests:** The authors declare that they have no competing interests. **Data and materials availability:** All data needed to evaluate the conclusions in the paper are present in the paper and/or the Supplementary Materials. Additional data related to this paper may be requested from the authors.

Submitted 19 June 2017
Accepted 16 February 2018
Published 6 April 2018
10.1126/sciadv.aao1470

Citation: P. Guillamat, Ž. Kos, J. Hardoüin, J. Ignés-Mullol, M. Ravnik, F. Sagués, Active nematic emulsions. *Sci. Adv.* **4**, eaao1470 (2018).

Downloaded from http://advances.sciencemag.org/ on April 7, 2018

ScienceAdvances

Active nematic emulsions

Pau Guillamat, Ziga Kos, Jérôme Hardoüin, Jordi Ignés-Mullol, Miha Ravnik and Francesc Sagués

Sci Adv **4** (4), eaao1470.
DOI: 10.1126/sciadv.aao1470

ARTICLE TOOLS http://advances.sciencemag.org/content/4/4/eaao1470

SUPPLEMENTARY MATERIALS http://advances.sciencemag.org/content/suppl/2018/04/02/4.4.eaao1470.DC1

REFERENCES This article cites 57 articles, 17 of which you can access for free
http://advances.sciencemag.org/content/4/4/eaao1470#BIBL

PERMISSIONS http://www.sciencemag.org/help/reprints-and-permissions

Use of this article is subject to the Terms of Service

Science Advances (ISSN 2375-2548) is published by the American Association for the Advancement of Science, 1200 New York Avenue NW, Washington, DC 20005. 2017 © The Authors, some rights reserved; exclusive licensee American Association for the Advancement of Science. No claim to original U.S. Government Works. The title *Science Advances* is a registered trademark of AAAS.

Downloaded from http://advances.sciencemag.org/ on April 7, 2018